

Lawrence Berkeley National Laboratory

LBL Publications

Title

Field validation of isotropic analytical models for simulating fabric shades

Permalink

<https://escholarship.org/uc/item/1b30r8m8>

Authors

Wang, Taoning

Lee, Eleanor S

Ward, Gregory J

et al.

Publication Date

2023-05-01

DOI

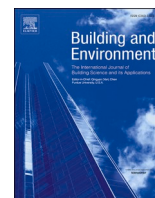
10.1016/j.buildenv.2023.110223

Copyright Information

This work is made available under the terms of a Creative Commons Attribution-NonCommercial-NoDerivatives License, available at

<https://creativecommons.org/licenses/by-nc-nd/4.0/>

Peer reviewed



Field validation of isotropic analytical models for simulating fabric shades

Taoning Wang^{a,*}, Eleanor S. Lee^a, Gregory J. Ward^b, Tammie Yu^a

^a Building Technologies and Urban Systems Division, Energy Technologies Area, Lawrence Berkeley National Laboratory (LBNL), Mailstop 90-3147, 1 Cyclotron Road, Berkeley, CA, 94720, USA

^b Anywhere Software, 950 Creston Road, Berkeley, CA, 94708, USA

ARTICLE INFO

Keywords:

Bidirectional scattering distribution function
Analytical fabric model
Daylighting
Complex fenestration systems
Windows
Discomfort glare

ABSTRACT

Fabric roller shades are common shading materials used in commercial and residential buildings. Accurately characterizing and modeling shades helps practitioners select the appropriate product and its control strategy based on climate and occupants' priorities, such as visual comfort and view to outdoors. Previous studies established a generalized method for modeling complex fenestration systems using data-driven tabulated bidirectional scattering distribution functions. However, deploying such a method at scale to all fabric shading products on the market is too costly and time-consuming. Analytical models that are based on a limited set of measurements (e.g., normal-normal and normal-hemispherical visible transmittance and reflectance, and directional cut-off angles) can be used to model the wide variety of shading products on the market. This study evaluates the performance of two isotropic analytical models, Roos-Wienold and Modified-Kotey, for modeling fabric roller shades, with a focus on the model's ability to predict occupant visual comfort. The performance evaluation was conducted through laboratory and field measurements and simulations. The results showed that both models are sufficient for predicting vertical illuminance at seated eye-level. Roos-Wienold model was able to predict binary visual comfort classification (glare/no-glare) under a wide range of luminance conditions, while Modified-Kotey model did not perform as well under high-contrast low-adaptation conditions. Both models are insufficient in predicting visual comfort at a four-point scale (e.g., imperceptible, perceptible, disturbing, intolerable). The two isotropic models become less accurate when the fabric exhibits high anisotropy.

1. Introduction

Fabric roller shades are in common use in commercial and residential buildings today due to architectural preferences such as ease of use and maintenance and aesthetic appearance. Simulating shades helps designers understand which fabrics to select to achieve an acceptable balance between solar control and daylight admission. With adequate control, shades can reduce lighting and heating, ventilation, and air conditioning (HVAC) energy use, helping to reduce the 4.33×10^{18} J (4.2×10^{15} Btus) or 3668 kWh per capita of primary energy attributable to windows in the United States [1]. Fabric shades must be modeled and controlled appropriately to increase user acceptance, comfort, and health, and to realize projected energy-savings potential. It is challenging to admit daylight and solar radiation in appropriate amounts and intensity at the right place and time to both lower electric lighting use and deliver daylight's health benefits while maintaining occupant comfort and minimizing window-induced HVAC loads. The performance

of each fabric shade product thus needs to be characterized accurately, so stakeholders can decide on the appropriate shading product and its control strategy for the specific climate, site, and building.

Fabric shades are particularly challenging to model due to their complex three-dimensional (3D) structure. Most fabric shades are made of coated threads woven together in various patterns. There can be multiple types of yarns of different colors and compositions in a single fabric. The coated yarn is often made of polyvinyl chloride or polyester, or a combination of both. Depending on its material and coating, each thread can be opaque or translucent in the visual and solar spectrum. Light of different incident directions interacts with the 3D structure of fabric thread differently, resulting in an optical transmission behavior that is highly angle dependent. Usually, maximum visible transmittance is at near normal incidence then decreases to zero as the incident direction approaches a grazing angle. Often, specular transmittance can reach zero before the angle of incidence reaches the grazing angle because the fabric's 3D structure blocks direct light.

Accurate characterization of specular transmission is a crucial

* Corresponding author.

E-mail address: taoningwang@lbl.gov (T. Wang).

Nomenclature		
θ, ϕ	incident angle ($^{\circ}$) in spherical coordinate with the sample in the xy plane (Figure A1)	$L_{s, e}$ m^2 peak glare source (solar) luminance (cd/m^2), determined by evalglare (e)
χ_{dir}	directional cut-off angle ($^{\circ}$)	$\omega_{s, e}$ peak glare source solid angle (sr), determined by evalglare (e)
$\tau_{v, n-h}$	normal-hemispherical visible transmittance	DGP daylight glare probability
$\tau_{v, n-n}$	normal-normal visible transmittance	(n)RMSE (normalized) root mean square error (%)
$\tau_{v, n-dif}$	normal-diffuse visible transmittance	(n)MAE (normalized) mean absolute error (%)
$\tau_{v, dir-h}$	angle dependent direct-hemispherical visible transmittance	(n)MBE (normalized) mean biased error (%)
$\tau_{v, dir-dir}$	angle dependent direct-direct visible transmittance	RMSE root mean square error
$\tau_{v, dir-dif}$	angle dependent direct-diffuse visible transmittance	MAE mean absolute error
$\tau_{v, dir-cone(5^{\circ})}$	direct-direct visible transmittance integrated over a 5° apex angle	MBE mean biased error
$\rho_{v, f, n-h}$	front normal-hemispherical visible reflectance	σ_n normalized standard deviation
$\rho_{v, b, n-h}$	back normal-hemispherical visible reflectance	c+a+ high-contrast and high-adaptation condition
$\rho_{v, dir-h}$	angle dependent direct-hemispherical visible reflectance	c+a high-contrast and low-adaptation condition
E_v	vertical illuminance (lx)	c-a+ low-contrast and high-adaptation condition
$L_{s, 2.5^{\circ}}$	average solar luminance evaluated at 2.5° apex angle (cd/m^2)	c-a low-contrast and low-adaptation condition
$L_{s, 5.0^{\circ}}$	average solar luminance evaluated at 5.0° apex angle (cd/m^2)	c combination of c-a+ and c-a- dataset
		RW Roos-Wienold analytical model (See Section 2.4)
		MK modified Kotey analytical model (See Section 2.5)

Table 1
Normal-normal (n-n) and normal-hemispherical (n-h) visible transmittance and reflectance and cut-off angle ($^{\circ}$) for fabrics with quadrilateral or 180° -rotational symmetry.

Fabric	$\tau_{v, n-h}$	$\tau_{v, n-n}$	$\rho_{v, f, n-h}$	$\rho_{v, b, n-h}$	$\chi_{dir}(0.005)^a$ ($^{\circ}$)	$\chi_{dir}(0.0)^b$ ($^{\circ}$)	Assumed symmetry and pglI measured angles of incidence (AOI)
BL1	0.173	0.015	0.791	0.781	135	120	Quadrilateral
BL3	0.194	0.029	0.776	0.774	130	110	
BL5	0.227	0.057	0.750	0.742	115	110	
BD1	0.010	0.007	0.082	0.089	150	120	
BD3	0.028	0.025	0.071	0.079	130	110	
BD5	0.052	0.048	0.073	0.081	120	110	
TL1	0.066	0.015	0.743	0.586	110	97.5	
TL3	0.110	0.048	0.72	0.607	110	97.5	
TD1	0.032	0.022	0.244	0.434	110	97.5	180° rotational
T'L1	0.154	0.004	0.437	0.322	90^c	97.5	
T'D1	0.031	0.003	0.105	0.263	90^c	97.5	

χ_{dir} derived from $\tau_{v, dir-cone(5^{\circ})}(\theta, \phi)$ threshold of 0 and 0.005 (EN14500).

^a $\chi_{dir}(\phi)$, where $\tau_{v, dir-cone(5^{\circ})}(\theta, \phi) < 0.005$. The directional cut-off angle χ_{dir} is the maximum $\chi_{dir}(\phi)$ for the measured ϕ . $\chi_{dir}(\phi)$ is the maximum incident θ whose $\tau_{v, dir-cone(5^{\circ})}(\theta, \phi)$ is less than 0.005.

^b $\chi_{dir}(\phi)$, where $\tau_{v, dir-cone(5^{\circ})}(\theta, \phi) = 0.0$. These data were not used in the RW model simulation. They are shown here to demonstrate how the threshold value affects the determination of the directional cut-off angle χ_{dir} .

^c $\tau_{v, dir-cone(5^{\circ})}(\theta, \phi) < 0.005$ for all θ

element in predicting occupants' visual comfort [2,3].¹ Previous studies have identified efficient simulation methods for computing luminance with complex fenestration systems, most recently [4,5]. Prior studies have also evaluated the accuracy of modeling specular transmission using data-driven, tabulated, Bidirectional Scattering Distribution Functions (BSDF) generated using an interpolation and peak extraction method defined by Refs. [3,6–8]. However, generating data-driven BSDFs is time-consuming and costly. It requires scanning a four-dimensional domain at sufficient resolution. Using a scanning goniophotometer to measure anisotropic optical properties of a fabric

¹ Modeling view out the window is also of interest to industry [12–15], but is outside the scope of this study.

shade can take many hours [9–11]. Given the variety of fabric shading products on the market, there is a need for a scalable solution that provides sufficiently accurate product data at moderate cost.

To this end, analytical models have been derived from detailed measurements of representative samples with the intent of extending their use to the entire class of fabric shading systems. Given the degree of simplification applied, measured inputs to the analytical model are significantly less and, for some models, can be conducted with standard bench-scale instrumentation used by the glazing industry to characterize solar transmission [7,16]. Prior studies evaluated the accuracy and shortcomings of such models for daylighting and glare analysis and identified the need for better and standardized procedures for characterizing fabric shades at scale [17–19].

This study evaluated two empirically-derived models: Roos-Wienold

(RW) [20] and modified-Kotey (MK) [16]. The RW model was used to derive design guidelines for the European daylighting standard [EN17037], and the MK model was adopted as part of the measurement and modeling protocol for the Attachment Energy Rating Council (AERC) [16]. The LBNL WINDOW library of AERC-designated shade fabrics has over 600 entries and has been publicly available at no cost to practitioners world-wide since 2016. The two models are both isotropic, meaning the optical properties were assumed to be rotationally invariant within the plane of the fabric; i.e., the grid structure and woven nature of the threads are assumed to have a negligible effect on overall optical properties. This study aims to evaluate the accuracy of these two analytical models against laboratory and field measurements, focusing on predicting visual comfort during the critical period when the solar disk is in the field of view.

2. Method

We evaluated absolute error by comparing: a) analytic versus laboratory-measured BSDF data for a hemispherical range of incident angles, and b) simulated data generated using the MK and RW models versus field-measured data for a limited range of incident angles. Fabric samples were measured and characterized using a scanning goniophotometer and evaluated in a full-scale testbed where vertical illuminance (E_v) and luminance of the solar disk region ($L_{s,2.5^\circ}$, $L_{s,5.0^\circ}$, $L_{s,e}$) and surroundings were measured using an illuminance meter and calibrated high dynamic range (HDR) imaging system. Simulated illuminance and luminance data were generated using the Radiance *rtrace* program and MK and RW input data. Discomfort glare (i.e., via daylight probability glare (DGP)²) was computed from measured and simulated HDR images.

2.1. Description of fabrics

This study included eleven woven fabric shades with a range of optical properties (Table 1). The fabrics were made of opaque polyester yarn or a combination of polyester and PVC coating and varied by color (light and dark shades of grey), weave (“basket” and “twill”), and openness factor (OF) (1%, 3%, and 5%). Fabric names were abbreviated with “WeaveColorOF.” For example, “BL1” represents the fabric with basket weave, light color, and 1% OF. The two types of twill weave fabrics were distinguished by an apostrophe ('). T' denotes twill weave fabrics made of 100% polyester threads, whereas T denotes twill weave fabrics made of 70% PVC and 30% polyester. The same set of fabrics is described in Ref. [6].

2.2. Characterization with scanning-goniophotometer

As summarized above, laboratory measurements of fabric samples were made to generate both the input data for the analytical models (Sections 2.4–2.5) and to evaluate model error (Section 3.1). Fabrics were measured using a scanning goniophotometer (Model “pgII,” Pab Advanced Technologies Ltd [9–11]) with a dynamic range of 70 dB and beam focused on the detector, as detailed in Refs. [3,6]. The symmetry property for each fabric was determined by visual inspection and determined to be quadrilaterally- or 180°-rotationally symmetric. Measurements were made at angles of incidence corresponding to each symmetry type (Table 1 diagrams). Transmittance and reflectance data

² The DGP metric was used in the analysis because it has been cross validated by independent field studies and found to deliver the highest performance and robustness amongst state-of-the-art metrics [21]. The metric includes a term that accounts for discrete sources of glare. A recent study [22] has validated the metric under conditions with direct sun in the field of view (authors acknowledged the need for further research, particularly the effect of strong spectral (color) shifts of glazing and CFS materials on glare). DGP has been adopted in the European daylighting standard EN17037.

were derived from measured data using Mountain software [11]. For the analytic models, normal-hemispherical and normal-normal visible transmittance, $\tau_{v,n-h}$ and $\tau_{v,n-n}$, data are given in Table 1 for cones with subtended angles of 180° and 5°, respectively. Cut-off angle data (χ_{dir}) used in the RW analytic model were derived using methods described in Section 2.4 below. To evaluate model error, direct-hemispherical and direct-direct visible transmittance, $\tau_{v,dir-h}(\theta, \varphi)$ and $\tau_{v,dir-cone(5^\circ)}(\theta, \varphi)$ were derived from the original pgII data (i.e., no interpolated angles of incidence). In this study, we used the Radiance convention for θ and φ (Figure A1), where $\varphi = 0^\circ$ points horizontally to the right, $\varphi = 90^\circ$ points upwards when viewing the front of the sample, and $\theta = 0-90^\circ$ denotes incident angles and $\theta = 180^\circ$ denotes outward scattering angles measured from the inward z-axis with the front of the sample facing towards the indoors.

2.3. Field measurements with HDR imaging system

Field measurements were conducted in a full-scale, outdoor testbed at LBNL in Berkeley, California, USA (37.87°N, 122.27°W). The experiment was conducted November 2–30, 2020 with incident solar angles within the range of: $\theta = 130-150^\circ$ and $\varphi = 30-160^\circ$. Direct normal and diffuse horizontal irradiance (DNI and DHI) were measured using a pyrheliometer (EKO MS-80, <0.2% non-linearity at 1000 W/m², spectral error $\pm 2\%$) and pyranometer (EKO MS-57, <0.2% non-linearity at 1000 W/m², spectral error $\pm 2\%$) mounted on a solar tracker. Measurements were performed under clear sky conditions with the sun in the camera’s field of view. Daily conditions were deemed to be sunny if DHI exhibited the typical smooth arc of a sunny day. Mean DNI and DHI varied by $\pm 4.6\%$ and $\pm 15.3\%$, respectively, between the 11 fabric test periods, indicating good comparability between the testing days’ solar condition. Summary solar conditions per fabric type are given in Figure A2.

The eleven fabrics were individually tested and mounted to fully cover a south-facing window (2.75 m \times 2.75 m) in a private office test chamber (3.05 m wide \times 4.57 m deep \times 3.05 m high). An HDR imaging system consisting of a full-frame, digital, single-lens reflex camera (Canon 5D) and a 180° fisheye lens (Sigma 8 mm) was mounted 1.0–1.5 m from the window, facing the window. Sequences of RAW format low dynamic range (LDR) images (3840 px \times 5760 px) were taken. They were later combined into HDR images (2000 px \times 2000 px) and calibrated using a separate spot luminance meter reading (Minolta LS110, 0.5° spot) taken simultaneous to HDR capture. To prevent pixel overflow, a neutral density filter was applied at the back of the fisheye lens. Vertical illuminance (E_v) was measured within 7 cm from the center of the fisheye camera lens using a cosine corrected, $v(\lambda)$ weighted, photometric sensor (Minolta T10, within 6% of $V(\lambda)$ and 3% of cosine response over 0.01–299,900 lx range). More details about the luminance and vertical illuminance measurements are provided in the previous study [6].

Data points where the window mullion obstructed the solar disk and circumsolar area (within an approximate apex angle of 5°) and shaded the sensors were removed. Data points where the HDR-derived E_v deviated more than 20% from the illuminance sensor measurement were also removed.

2.4. Modeling with the Roos-Wienold model

The original Roos model [23] was developed for specular glass, where the formula for angle-dependent, direct-direct transmittance, $\tau_{v,dir-dir}(\theta)$, is:

$$\tau_{v,dir-dir}(\theta) = \tau_{v,n-n} * \left(1 - 8 \zeta^\alpha - \frac{0.25}{q} \zeta^2 - \left(1 - 8 - \frac{0.25}{q} \right) \zeta^\gamma \right), \quad (1)$$

where,

$$\zeta = \frac{\theta}{90^\circ}$$

$$\alpha(q) = 5.2 + 0.7q$$

$$\gamma(p, q) = 5.26 + 0.06p + 0.73q + 0.04pq,$$

and where p is the number of panes in the window configuration and q is the material category of the coating defined in Ref. [23].

Wienold adapted this model to fabric shades by incorporating a directional cut-off angle [20]. As a result, the parameters ζ , p , and q were modified in Equation (1), where $p = 4$, $q = 2.9$, and

$$\zeta = \frac{\theta}{90^\circ} + 1 - \frac{\chi_{dir}}{90^\circ} \quad (2)$$

where χ_{dir} is the cut-off angle (i.e., incident grazing angle within $\theta = 0-90^\circ$ range). The determination of the directional cut-off angle followed EN14500. The directional cut-off angle for each φ angle, $\chi_{dir}(\varphi)$, was determined when $\tau_{v, dir-cone(5^\circ)}(\theta, \varphi) < 0.005$. The directional cut-off angle for the fabric, χ_{dir} , was $\max[\chi_{dir}(\varphi)]$ among the measured φ angles. Modeling using the RW model required measuring the fabric at many rotational φ angles, even though the model assumed isotropic behavior. Measurement requirements are discussed further in Section 4.4 and implications of (an)isotropy are discussed in Section 4.1.

To model fabrics using the RW model, we derived $\tau_{v, n-h}$ and $\tau_{v, n-n}$ from the pglI normal incidence, front-to-back transmission data integrated at a cone of 180° and 5° , respectively. $\tau_{v, n-dif}$ is the difference between $\tau_{v, n-h}$ and $\tau_{v, n-n}$. Similarly, front and back hemispherical reflectance values ($\rho_{v, f, n-h}$ and $\rho_{v, b, n-h}$) were also derived from the pglI data.

In *Radiance*, the RW model was implemented as a *BRTDfunc* material type, as it was originally modeled in Ref. [20]. This material type models the specular component without forward scattering. So to counteract the limitation of this material type, the RW model defines $\tau_{v, n-n}$ as integrated over a 5° apex angle, which includes the shoulder (forward scattering) region of the direct-direct transmission. The diffuse component is Lambertian. Both specular and diffuse components are attenuated by the glazing layer according to Fresnel equation with a transmissivity of 1.0 and refraction index of 1.05, which means that transmittance was reduced by 1% up to 65° , 5% at 72° , 20% at 80° , and 50% at 85° AOI. Solar disk in each rendering was subsequently blurred using the same blurring function defined in Refs. [3,6], based on the human retinal blurring function, which also approximated the scattering of the camera lens.

2.5. Modeling with Modified-Kotey model

The MK model was developed based on the original Kotey model [24] and later adapted for AERC [16]. The coefficients to the original Kotey model were modified based on measured data for 60 fabric samples using an integrating sphere and angle tube [16]. The inputs to the MK model were normal incidence measurements: $\tau_{v, n-n}$, $\tau_{v, n-dif}$, and $\rho_{v, n-n}$. Like the RW model, the MK model also assumed isotropic behavior. The model defined the angle-dependent transmittance as:

$$\tau_{v, dir-dir}(\theta) = \tau_{v, n-n} \cos^b(\theta) \quad (3)$$

$$\tau_{v, dir-dif}(\theta) = \tau_{v, n-dif} \cos^{bd}(\theta) \quad (4)$$

Where the exponent variables b and bd are given by

$$b = \max[-0.35 \ln(\max[\tau_{v, n-n}, 0.01]), 0.35]$$

$$bd = \max[-0.35 \ln(\max[\tau_{v, n-dif}, 0.01]), 0.35],$$

respectively. Reflectance was modeled as

$$\rho_{v, dir-h}(\theta) = \rho_{v, n-h} + (\rho_{Kotey(90^\circ)} - \rho_{v, n-h}) (1 - \cos^{0.6}(\theta)) \quad (5)$$

where $\rho_{Kotey(90^\circ)}$ is defined as:

$$\rho_{Kotey(90^\circ)} = \rho_{v, n-h} + (1 - \rho_{v, n-h}) (0.7\rho_y^{0.7})$$

and ρ_y is defined as

$$\rho_y = \rho_{v, b, n-h} / (1 - \tau_{v, n-n})$$

The $\tau_{v, n-h}$, $\tau_{v, n-dif}$, $\tau_{v, n-n}$, and $\rho_{v, b, n-h}$ were derived from the measured pglI data in the same manner as described in Section 2.4.

The *Radiance* tool *bsdf2tree* was used to produce the tabulated tensor tree BSDF [25] based on Equations (3)–(5), where options *-t 4* and *-g 6* were used to invoke anisotropic sampling and set a tensor tree resolution of $2^6 \times 2^6$. Anisotropic sampling avoided a minor issue we had with *-t 3* in-plane tensor tree peaks, which was a potential source of systematic errors. Since the modified-Kotey model was isotropic, the resulting tabulated BSDF was still isotropic.³ A *Radiance .cal* file was used to define the optical behavior according to the modified-Kotey model (Equations (3)–(5)). Rays were sent and sampled during the generation of the tensor tree BSDF, where specular rays were determined by whether the scattered rays were within the 0.533° apex angle centered around the “through” ray. Peak extraction was turned on for MK datasets to model the specular view component except for BL1 [26]. BL1, despite having a 1% openness factor, could not be seen through, and objects on the other side could not be distinguished. The same blur function mentioned above was applied to the MK model.

2.6. Simulation and glare evaluation

The RW model was implemented with *Radiance BRTDfunc* material [20], while the MK model used a BSDF tabulated data [16]. This introduced an inherent bias due to the former model yielding continuous data versus discrete (tabulated) data of the latter. Notwithstanding, both simulation methods adhered to that of the original studies. E_v values for each fabric were generated using the *Radiance rtrace* program at a 2-min interval. Renderings with a resolution of 2000 px by 2000 px were also generated with the *rtrace* program at a 10-min interval. *Rtrace* simulations were run with *-ab 6 -ad 512 -aa 0*. The simulation sky model was generated using *Radiance gendaylit* program, which is based on the Perez All-Weather model [27].

For both measured and simulated images, the *Radiance evalglare* program (v2.10) [28] was used to compute each rendering's glare source luminance and DGP. Glare sources were identified with a threshold of 2000 cd/m^2 , and a separate peak glare source was identified with a threshold of $5.0 \times 10^4 \text{ cd/m}^2$. No task area was identified, given the view of facing normal to the window. The dataset was classified into contrast-based and saturation-based discomfort glare, where contrast-based glare was caused by an excessive bright glare source in a relatively dimly lit environment and saturation-based glare was caused by an overall bright luminance at the eye. The DGP equation is

$$DGP = 5.87 * 10^{-5} \underbrace{E_v}_{\text{saturation term}} + 9.18 * 10^{-2} \log_{10} \left(1 + \underbrace{\frac{\sum_{i=0}^n L_{s,i}^2 * \omega_{s,i}}{E_v^{1.87} * P_{s,i}^2}}_{\text{contrast term (log_gc)}} \right) + 0.16 \quad (6)$$

where the first part of the equation (E_v) accounted for the saturation (adaptation) effect and second term (\log_{gc}) for the contrast effect. A 0.5

³ Selection of this tensor tree resolution provides error estimates that are comparable to prior validation studies. For simulations with lower resolution BSDFs, errors may increase.

Table 2

$\tau_{v, dir-h}(\theta, \phi)$ error of RW and MK models compared to pgII-derived data for measured incident angles shown in Table 1.

Θ range	Data count	r^2	RMSE	nRMSE	MAE	nMAE	MBE	nMBE
RW								
180–90°	613	0.98	0.0100	13.7%	0.0066	9.06%	0.0052	7.14%
180–150°	194	1.00	0.0044	4.85%	0.0030	3.31%	0.0014	1.54%
150–120°	296	0.98	0.0110	15.5%	0.0073	10.3%	0.0058	8.18%
120–90°	123	0.97	0.0150	30.3%	0.0100	20.2%	0.0095	19.2%
MK								
180–90°	613	0.96	0.0150	20.6%	0.0098	13.4%	-0.0061	-8.37%
180–150°	194	1.00	0.0040	4.41%	0.0033	3.64%	-0.0011	-1.21%
150–120°	296	0.98	0.0130	18.3%	0.0110	15.5%	-0.0055	-7.76%
120–90°	123	0.93	0.0260	52.5%	0.0180	36.3%	-0.0150	-30.3%

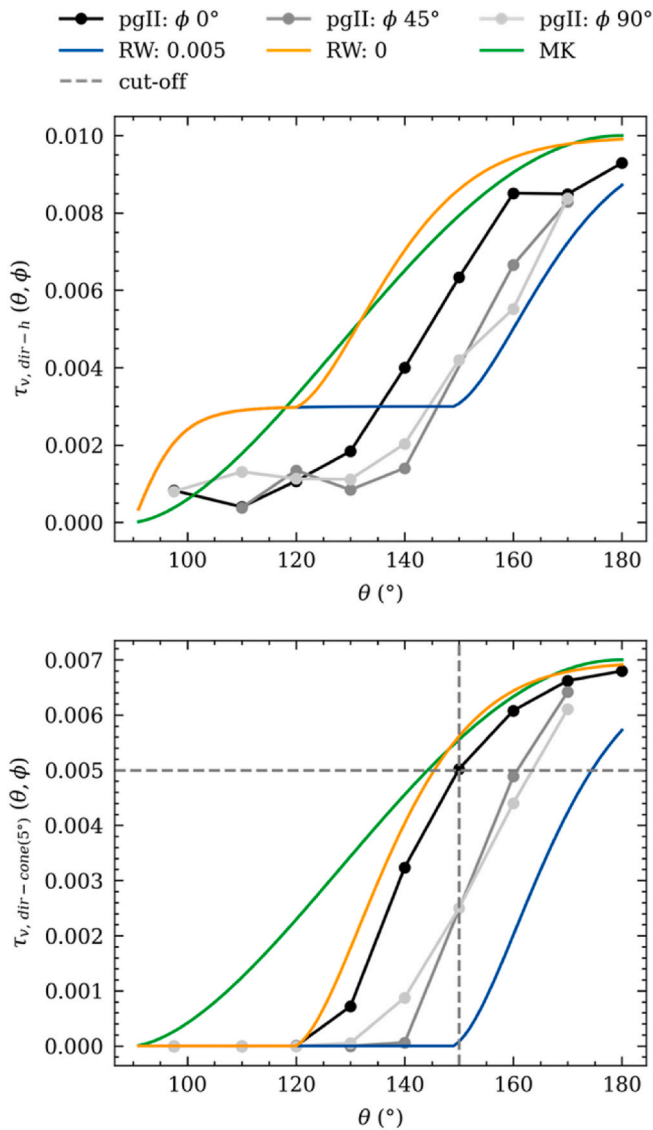


Fig. 1. Comparison between BD1’s analytical model and pgII-derived data at incident $\phi = 0^\circ, 45^\circ,$ and 90° for direct-hemispherical (top) and direct-direct (bottom) visible transmittance. Per EN14500, BD1’s $\chi_{dir} = 150^\circ$, which is the maximum θ from normal incidence angle and where the pgII $\tau_{v, dir-cone(5^\circ)}(\theta, \phi)$ (grayscale) and cut-off (dashed line) lines intersect. The RW: 0.005 (blue line) function was modeled with $\tau_{v, dir-cone(5^\circ)}(\theta, \phi)$ threshold 0.005 and $\chi_{dir} = 150^\circ$. The RW: 0 (orange line) function was modeled with $\tau_{v, dir-cone(5^\circ)}(\theta, \phi)$ threshold 0 and $\chi_{dir} = 120^\circ$. (For interpretation of the references to color in this figure legend, the reader is referred to the Web version of this article.)

log_{gc} threshold and 3000 lx E_v threshold were used to divide the datasets into high/low contrast and high/low adaptation levels, respectively [29]. The measured dataset for the eleven fabric shades was categorized into four conditions: high-contrast-high-adaptation (c+a+), high-contrast-low-adaptation (c+a-), and low-contrast-high-adaptation (c-a+) and low-contrast-low-adaptation (c-a-). Because there were only two data points under c-a- conditions, a single low-contrast (c-) category was used to represent both c-a- and c-a+. Most of the c-data points were from BL1 fabric. In addition to DGP, $L_{s,e}$ and $\omega_{s,e}$ was also computed with the *evalglare* program. $L_{s,e}$ and $\omega_{s,e}$ values were extracted from the peak glare source where the average peak luminance was greater than 5.0×10^4 cd/m². These peak glare sources were manually examined to ensure they all represented solar disks in the HDR images. $L_{s,2.5^\circ}$ and $L_{s,5.0^\circ}$ were extracted at the solar disk location at 2.5° and 5.0° apex angle in each image.

3. Results

3.1. Comparison to pgII measurements

Comparisons were made between the analytical model and reference pgII-derived data for a total of 613 measured incident angle locations (Table 1 diagram) collected across the eleven fabrics. Errors were determined for the entire dataset and for subsets of data at 30° θ intervals. The results are presented in the following sections for direct-hemispherical and direct-direct visible transmittance. In addition, the anisotropy and its relation to the error of each fabric were also analyzed.

3.1.1. $\tau_{v, dir-h}(\theta, \phi)$ error

The analytical models were found to be most aligned with the pgII dataset near the normal angle of incidence and deviated as the incident angle increased (Table 2 and Fig. 1, top for example fabric BD1). For incident θ from 180 to 150°, 150–120°, and 120–90°; the MAE for the RW dataset were 3.3%, 10.3%, and 20.2%, respectively; and 3.6%, 15.5%, and 36.3% for the MK dataset, respectively (Table 2). The overall $\tau_{v, dir-h}(\theta, \phi)$ correlation for incident $\theta = 180-90^\circ$ was good, with $r^2 = 0.98$ and 0.96 for the RW and MK datasets, respectively. For this section of analysis, the comparisons were useful for identifying general trends in error associated with the analytical models. Sub-analysis based on material properties (dark/light fabric, openness factor) was performed in Section 3.2 and related to data in Section 3.1.

3.1.2. $\tau_{v, dir-cone(5^\circ)}(\theta, \phi)$ error

We observed similar trends with $\tau_{v, dir-cone(5^\circ)}(\theta, \phi)$ where agreement between model- and pgII-derived datasets was best near normal and decreased as the angle of incidence increased (Table 3; Fig. 1, bottom). The difference between the RW model and pgII-derived transmittance was explained above. For $\theta = 180-150^\circ$, both models performed well, with a MAE of 8.6% and 10.1% for the RW and MK models, respectively. MK model MAE drastically increased to 86.5% and 1450.0% with $\theta = 150-120^\circ$ and $\theta = 120-90^\circ$. The RW model, on the other hand, performed relatively better with a corresponding MAE of 31.5% and

Table 3

$\tau_{v, \text{dir-cone}(5^\circ)}(\theta, \phi)$ error of RW and MK models compared to pgII-derived data for measured incident angles shown in Table 1.

Θ range	Data count	r^2	RMSE	nRMSE	MAE	nMAE	MBE	nMBE
RW								
180–90°	613	0.96	0.0029	29.0%	0.00180	18.0%	0.00023	2.30%
180–150°	194	0.98	0.0026	13.2%	0.00170	8.62%	−0.00014	−0.71%
150–120°	296	0.88	0.0036	47.2%	0.00240	31.5%	0.00054	7.08%
120–90°	123	0.00	0.0013	44.0%	0.00049	16.6%	0.00004	12.20%
MK								
180–90°	613	0.79	0.0073	73.1%	0.0047	47.1%	0.00350	35.10%
180–150°	194	0.98	0.0027	13.7%	0.0020	10.1%	0.00059	2.99%
150–120°	296	0.55	0.0093	122.0%	0.0066	86.5%	0.00520	68.20%
120–90°	123	0.02	0.0066	2230%	0.0043	1450%	0.00410	1390%

Table 4

Normalized standard deviation (σ_n) of pgII-derived $\tau_{v, \text{dir-h}}(\theta, \phi)$ and $\tau_{v, \text{dir-cone}(5^\circ)}(\theta, \phi)$ at $\theta = 140^\circ$, and corresponding nMAE (%) from the analytical models. Fabrics that had higher σ_n , also were more anisotropic and had higher nMAE(%) in $\tau_{v, \text{dir-h}}(\theta, \phi)$ and $\tau_{v, \text{dir-cone}(5^\circ)}(\theta, \phi)$ at $\theta = 140^\circ$, compared to pgII measurements.

	condition	$\sigma_n, \text{dir-h}$	$\tau_{v, \text{dir-h}}(\theta, \phi)$		$\sigma_n, \text{dir-cone}(5^\circ)$	$\tau_{v, \text{dir-cone}(5^\circ)}(\theta, \phi)$	
			nMAE (%)			nMAE (%)	
			RW	MK		RW	MK
BL1	c-a+	0.0101	4.2	13.9	0.7480	18.8	101.0
BL3	c+a+	0.0062	2.8	11.6	0.1620	14.2	65.6
BL5	c+a+	0.0094	1.6	7.8	0.1120	12.2	48.8
BD1	c+a-	0.3720	53.1	89.5	1.1700	62.4	123.0
BD3	c+a-	0.1700	11.6	58.7	0.2290	8.7	80.9
BD5	c+a-	0.1510	17.9	46.3	0.1950	16.9	54.3
T'L1	c+a+	0.0272	15.0	12.1	0.0581	29.6	30.6
TL1	c+a-	0.0425	18.0	13.3	0.2410	24.0	31.2
TL3	c+a+	0.0214	12.9	5.6	0.0498	16.8	26.2
T'D1	c+a-	0.0800	19.1	27.1	0.1460	34.7	45.7
TD1	c+a-	0.0875	15.4	18.3	0.2300	19.8	32.5

166.0%. RW had a better overall correlation with pgII-derived data, with $r^2 = 0.96$ in comparison to MK's $r^2 = 0.79$ (Table 4). MK's relatively worse correlation occurred mainly at oblique angles of incidence between $\theta = 150-120^\circ$ and $\theta = 120-90^\circ$, $r^2 = 0.55$ and 0.02 , respectively. The RW model also had a smaller MBE of +2.3% ($\theta = 180-90^\circ$), as opposed to the +35.1% overestimation of the MK model. The better performance from the RW model can be attributed to the additional χ_{dir} parameter, modeling the reduction in transmission due to the fabric cut-off angle.

3.1.3. Anisotropy

Both RW and MK models assumed isotropic optical behavior, modeling $\tau_{v, \text{dir-h}}(\theta, \phi)$ and $\tau_{v, \text{dir-cone}(5^\circ)}(\theta, \phi)$ as a function of θ and not ϕ . In the real world, the 3-D woven nature of fabrics indicated that they were indeed anisotropic, and different fabrics exhibited different levels of anisotropy. We characterized the anisotropy of each fabric by calculating the normalized standard deviation (σ_n) of pgII-derived $\tau_{v, \text{dir-h}}(\theta, \phi)$ ($\theta = 140^\circ$) and $\tau_{v, \text{dir-cone}(5^\circ)}(\theta, \phi)$ ($\theta = 140^\circ$) across all ϕ angles. The $\theta = 140^\circ$ angle was chosen because we had sufficient non-zero (before cut-off) data at this angle for all fabrics. This σ_n informed us of the spread in $\tau_{v, \text{dir-h}}(\theta, \phi)$ and $\tau_{v, \text{dir-cone}(5^\circ)}(\theta, \phi)$ at $\theta = 140^\circ$; the higher the σ_n , the more anisotropic the fabric was. Overall, we observed that dark colored fabrics were more anisotropic than their light-colored counterparts. Fabrics that had smaller openness factors were also more anisotropic. We also observed that the errors in $\tau_{v, \text{dir-h}}(\theta, \phi)$ and $\tau_{v, \text{dir-cone}(5^\circ)}(\theta, \phi)$ were positively correlated the degree of anisotropic behavior (proxied by σ_n) (Fig. 2). Table 4 lists the σ_n of each fabric and their associated $\tau_{v, \text{dir-h}}(\theta, \phi)$ and $\tau_{v, \text{dir-cone}(5^\circ)}(\theta, \phi)$ MAE comparing the values measured using pgII. As shown in Fig. 2, for both RW and MK models, MAE increased with σ_n . Note RW MAE was significantly lower than that of MK with increased anisotropic behavior.

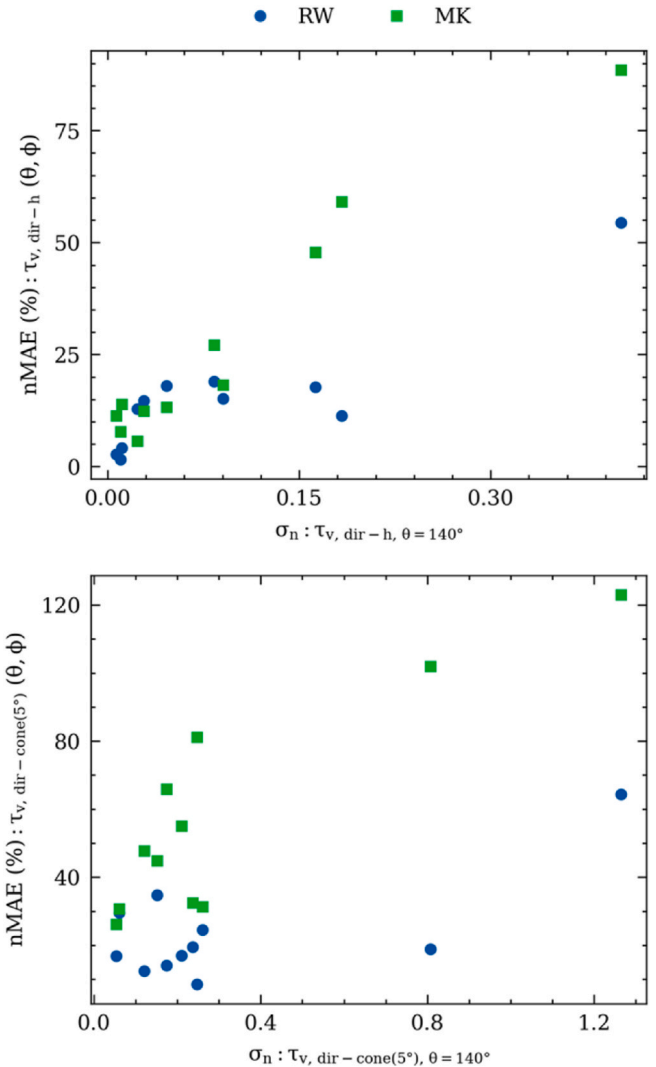


Fig. 2. Positive correlation between MAE and normalized standard deviation (σ_n) of pgII-derived $\tau_{v, \text{dir-h}}(\theta, \phi)$ and $\tau_{v, \text{dir-cone}(5^\circ)}(\theta, \phi)$ at $\theta = 140^\circ$. Each datapoint represents one of the eleven measured fabrics.

3.2. Comparison to field measurements

We evaluated the error of the two analytical models against field measurement with the lighting conditions broken down into three categories: high contrast, high adaption (c+a+), high contrast, low adaptation (c+a-), and low contrast (c-). Most of the fabrics exhibited the specular view component (with a visible solar disk), and thus were in high contrast scenarios. BL1 was the only fabric that exhibited low-

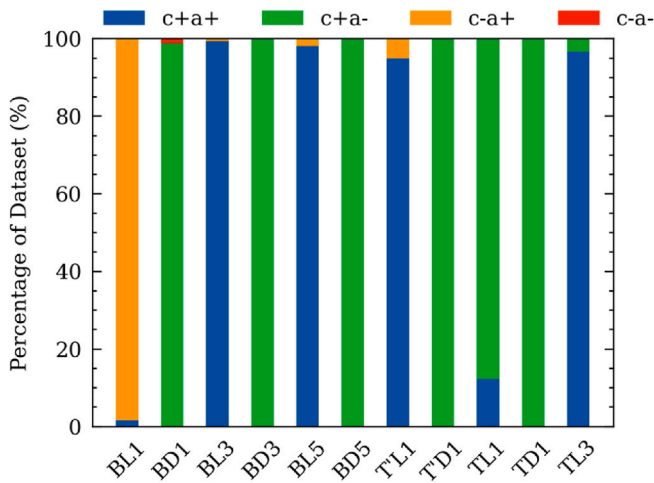


Fig. 3. Classification of the measured HDR images for each fabric.

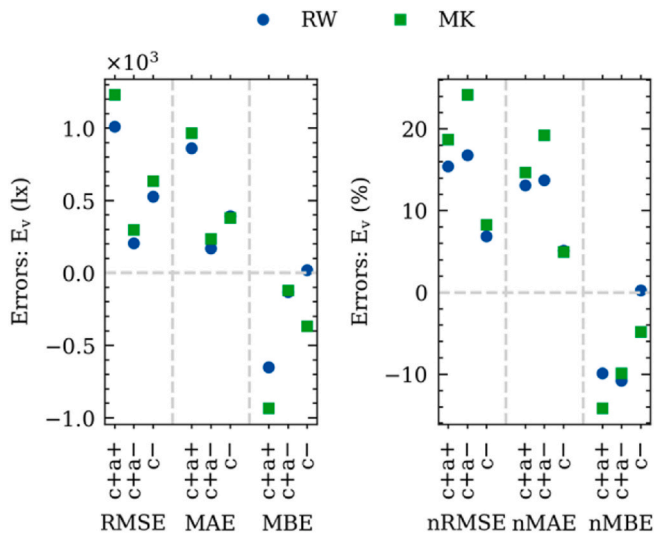


Fig. 4. E_v RMSE, MAE, and MBE breakdown by adaptation and contrast conditions: c+a+, c+a-, and c-.

contrast levels and had no direct view component. The light-colored fabrics produced mostly high adaptation conditions, whereas the dark-colored fabrics produced low-adaptation conditions, except T'L1 (Fig. 3). In the following sections, we evaluated the energy conservation in illuminance and solar luminance, followed by a performance evaluation in predicting visual comfort for the two models.

Note that the field validation captured a limited subset of all possible solar conditions due to time and location of measurements, geometry of room and window, south-facing orientation, and site location.

3.2.1. Energy conservation: vertical illuminance

A total of 2066 E_v data points were collected in the outdoor testbed across the eleven fabrics, with the measured E_v ranging from 58 lx to 12830 lx and a median of 4052 lx. For the RW model, RMSE, MAE, and MBE errors for E_v were 681 lx, 468 lx, and -345 lx, normalizing to 18.2%, 12.5%, and -9.2%, respectively. For the MK model, RMSE, MAE, and MBE errors were 837 lx, 548 lx, and -475 lx, normalizing to 22.4%, 14.6%, and -12.7%, respectively (Table A1). Under all contrast-adaptation conditions, RW simulated results showed better agreement with the field measurements than MK results. Overall, light-colored fabrics (c+a+) had a smaller distribution in E_v difference than dark-colored fabrics (c+a-) (Fig. 5). The light-colored fabrics had diffuse

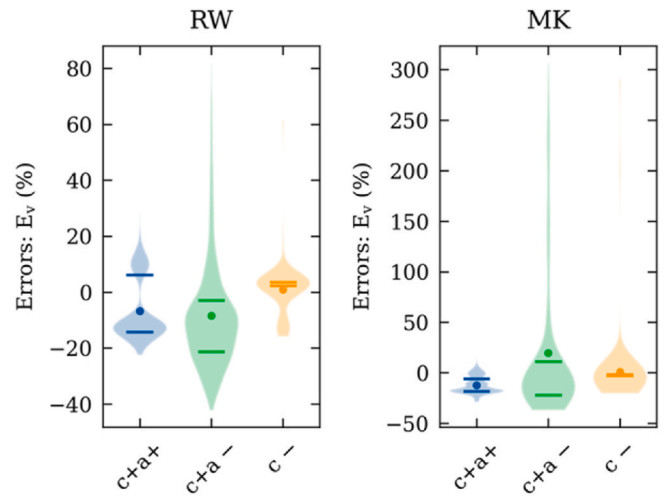


Fig. 5. Data distribution for E_v difference between the measurement and analytical model simulation, breakdown by contrast-adaptation condition: c+a+, c+a-, and c-. The bars denote the 25% and 75% quartiles, and the dot denotes the mean. The outliers in c+a- and c- were from BD1.

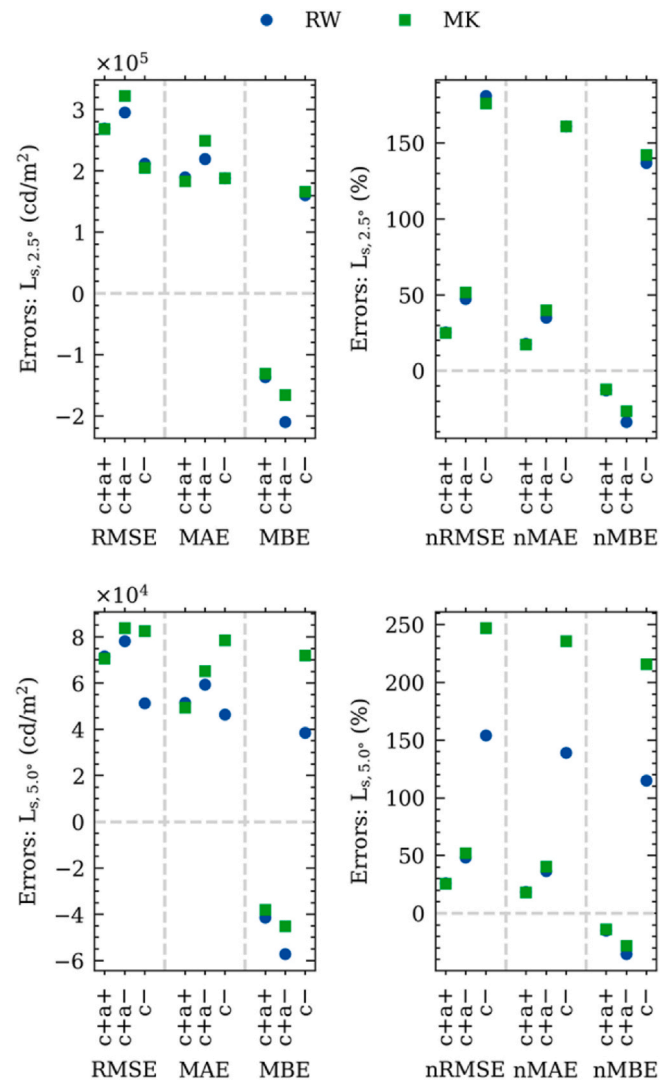


Fig. 6. Solar luminance evaluated at 2.5° and 5.0° apex angles ($L_{s,2.5^\circ}$ and $L_{s,5.0^\circ}$) RMSE, MAE, and MBE breakdown by adaptation and contrast conditions: c+a+, c+a-, and c-.

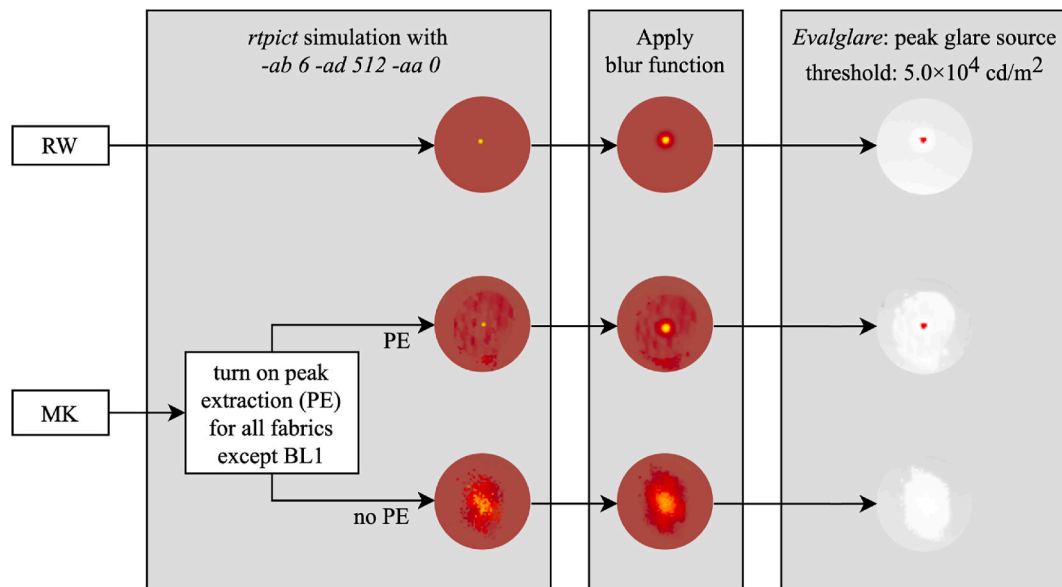


Fig. 7. Radiance *rtrace* (through *rt pict*) program generated HDR renderings for the RW and MK model, with the solar disk at a 0.533° apex angle. Then, the blur function was applied to the rendered HDR to account for the HDR camera scattering. The Radiance *evalglare* program evaluated solar glare source whose luminance is greater than $50,000 \text{ cd/m}^2$.

transmittance largely influencing E_v and were less sensitive to changes in angles of incidence. The opposite was true for darker fabrics, where most of the E_v was from direct transmittance. The negative mean bias error indicated an overall underestimation of E_v . The E_v error breakdown by adaptation and contrast conditions is shown in Fig. 4. E_v error summary tables are included in the Appendix. Overall E_v agreement for each model is shown in Fig. 11 (a, g).

3.2.2. Energy conservation: solar luminance

RW and MK models were rendered at a 10-min interval for luminance calculations, resulting in a total of 497 images for the eleven fabrics. In the RW dataset, RMSE, MAE, and MBE errors for solar luminance evaluated at 2.5° apex angles ($L_{s,2.5^\circ}$) were $2.79 \times 10^5 \text{ cd/m}^2$, $2.05 \times 10^5 \text{ cd/m}^2$, and $-1.52 \times 10^5 \text{ cd/m}^2$, normalizing to 36.4%, 26.7%, and -19.8% , respectively. The negative MBE indicated an overall underestimation. For the MK dataset, RMSE, MAE, and MBE errors were $2.93 \times 10^5 \text{ cd/m}^2$, $2.18 \times 10^5 \text{ cd/m}^2$, $-1.27 \times 10^5 \text{ cd/m}^2$, normalizing to 38.2%, 28.3%, -16.5% , respectively (Table A2). Similar correlation trends were found with $L_{s,5.0^\circ}$ (Table A3). Overall $L_{s,2.5^\circ}$ and $L_{s,5.0^\circ}$ agreements for each model are shown in Fig. 11 (b, c, h, i).

Breaking down the datasets by contrast levels, we observed overestimation with low-contrast cases and slight underestimation with high-contrast cases, for both models. With high-contrast scenarios, both models performed better with c+a+ and had trouble with c+a-cases (Fig. 6).

RW model performed well in c+a+ cases, with a MAE of 17.8% and 18.6% for the $L_{s,2.5^\circ}$ and $L_{s,5.0^\circ}$, respectively; but performed worse under c+a-cases, with a MAE of 35.1% and 36.7% for $L_{s,2.5^\circ}$ and $L_{s,5.0^\circ}$ respectively. One fabric that RW had difficulty in modeling was BD1, as shown in Fig. 11 (b, c), the cluster of green data points on the lower left corner. The underestimation and “flat” profile could be explained by the early cut-off of the specular component, as shown in Fig. 1 (bottom). RW model (in blue) decreased to zero in the field measurement range ($\theta = 135\text{--}149^\circ$ and $\phi = 30\text{--}150^\circ$); as a result, there was no visible solar disk in the rendering. The inaccuracy of the RW model could be partly explained by the determination of the cut-off angle, which is discussed later.

Similarly, MK performed better in c+a+ than in c+a-cases. For c+a+ cases, MAE were 17.2% and 17.9% for $L_{s,2.5^\circ}$ and $L_{s,5.0^\circ}$ respectively. MK MAE for c+a-were slightly worse than RW's, at 39.9% and 40.3% for

$L_{s,2.5^\circ}$ and $L_{s,5.0^\circ}$, respectively. Like RW, MK also did not perform well with BD1, as shown in Fig. 11 (h, i), where there was a large deviation with measured $L_{s,2.5^\circ}$ ranging from 3×10^3 to $1 \times 10^5 \text{ cd/m}^2$. As shown in Fig. 1 (bottom), MK (in green) overestimated $\tau_{v, \text{dir-cone}(5^\circ)}(\theta, \phi)$ in the pgII measurement range ($\theta = 140\text{--}150^\circ$ and $\phi = 45\text{--}90^\circ$).

Both RW and MK greatly overestimated $L_{s,2.5^\circ}$ and $L_{s,5.0^\circ}$ for the c-case, which was primarily composed of the BL1 dataset. We observed no direct component in the field HDR measurements, i.e., the solar disk was not visible through the fabric. However, BL1 was measured by pgII to have a specular transmission (1.5%); thus, both analytical models had specular transmission. This discrepancy between field and pgII measurements was likely caused by fabric sample differences. We discuss this in the Section 4.

3.2.3. Glare prediction

Given that this study focuses on scenarios with the solar disk in the field of view, the dominating factors contributing to glare were E_v , $\omega_{s,e}$, and $L_{s,e}$, the solid angle and mean glare source luminance in the solar disk region where pixel values exceeded $50,000 \text{ cd/m}^2$. Overall agreements in $L_{s,e}$, $\omega_{s,e}$, and DGP for each model are shown in Fig. 11 (d, e, f, j, k, l).

$L_{s,e}$ had RMSE and MAE of $5.59 \times 10^5 \text{ cd/m}^2$ (45.4%) and $4.81 \times 10^5 \text{ cd/m}^2$ (39.0%) for the RW dataset, and $4.43 \times 10^5 \text{ cd/m}^2$ (36.0%) and $3.58 \times 10^5 \text{ cd/m}^2$ (29.1%) for the MK dataset. BD1 was excluded in the $L_{s,e}$ and $\omega_{s,e}$ analysis because the solar disk was not in the field of view in the RW's simulated HDR, i.e., no pixels in the solar disk region with luminance $>50,000 \text{ cd/m}^2$. Both models overestimated $L_{s,e}$, with an MBE of $4.34 \times 10^5 \text{ cd/m}^2$ (35.3%) and $2.52 \times 10^5 \text{ cd/m}^2$ (20.5%) for the RW and MK dataset, respectively. The low-contrast fabrics, which were mainly composed of BL1, had the largest MAE: $8.53 \times 10^5 \text{ cd/m}^2$ (387.0%) and $9.85 \times 10^4 \text{ cd/m}^2$ (44.7%) for the RW and MK dataset, respectively (Table A4). The relatively large errors with c-cases were also related to sample differences as mentioned in Section 3.2.2. $L_{s,e}$ error for each contrast-adaptation condition is shown in Fig. 8 (top).

In contrast to the overestimated $L_{s,e}$ term, the solid angle of all pixels $>50,000 \text{ cd/m}^2$ in the solar disk region, $\omega_{s,e}$, was under-predicted. For both models, the solar disk was first rendered to be a pure specular component, with a size of 0.533° apex angle (the apex angle of the solar disk). The solar disk was then blurred as described in Sections 2.3 and 2.4 (Fig. 7). For the RW dataset, the overall, c+a+, c+a-, and c- MBE

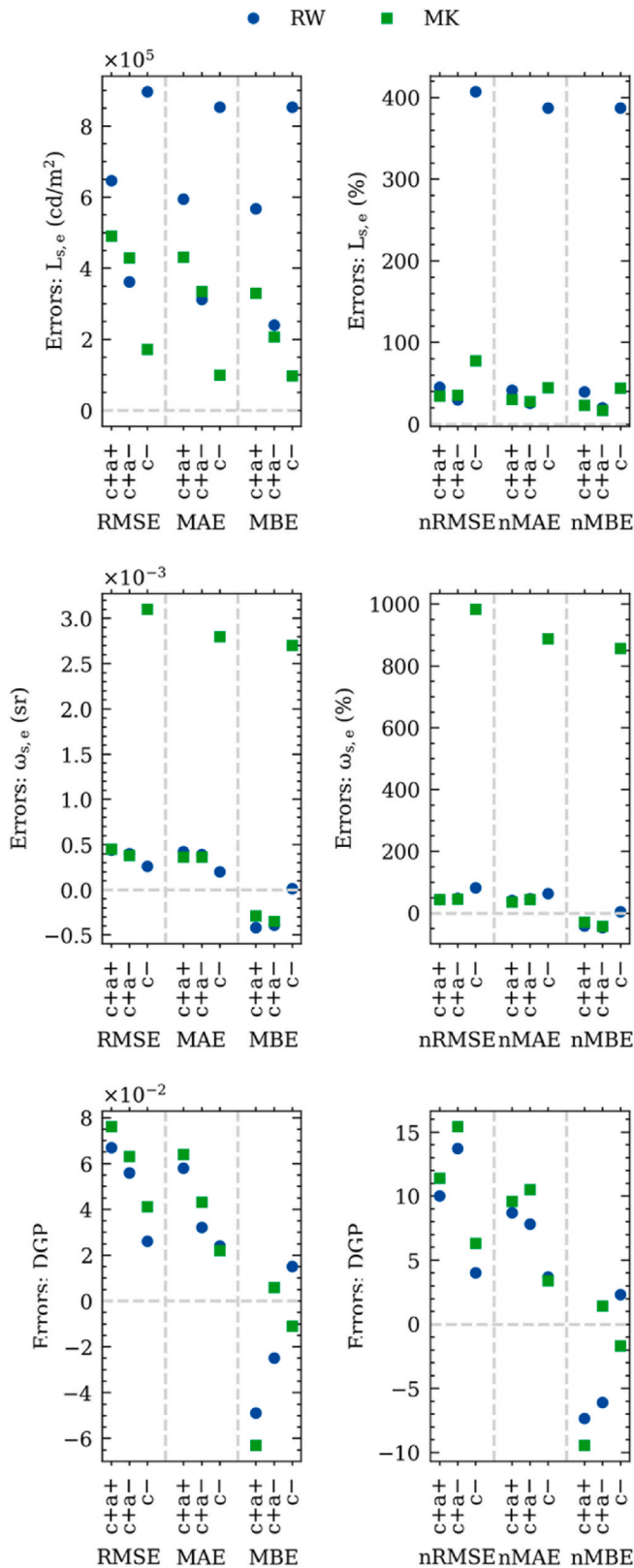


Fig. 8. Peak glare source (solar) luminance, solid angle, and DGP RMSE, MAE, and MBE breakdown by adaptation and contrast conditions: c+a+, c+a-, and c-.

were -42.7%, -41.7%, -46.9%, and 4.3%, respectively. For the MK dataset, the overall, c+a+, c+a-, and c- MBE were -9.3%, -29.2%, -42.2%, and 854.0%, respectively. The c-condition (BL1) had a positive bias for the same reason explained above. The c + condition

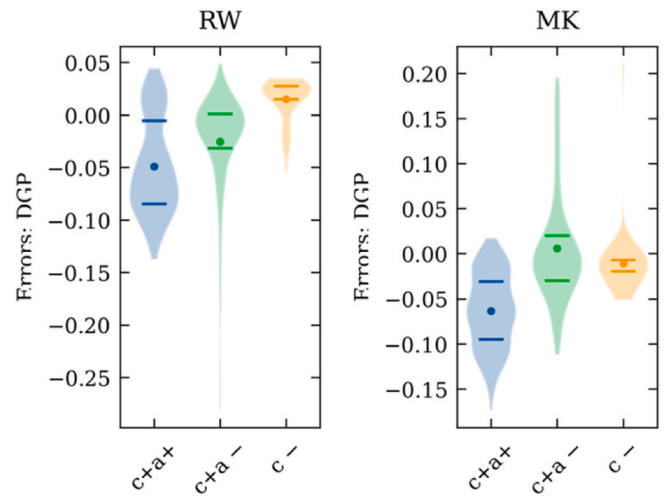


Fig. 9. Data distribution for DGP difference between the field measurement and analytical model simulation, breakdown by contrast-adaptation condition: c+a+, c+a-, and c-. The bars denote the 25% and 75% quartiles, and the dot denotes the mean. The outliers in c+a- and c- were from BD1.

underestimated $\omega_{s,e}$ due to fewer pixels over 5×10^4 cd/m^2 detected in the simulated images compared to the measured images. $\omega_{s,e}$ error for each contrast-adaptation condition is shown in Fig. 8 (middle).

Despite the large errors in $L_{s,e}$ and $\omega_{s,e}$, simulated DGP agreed relatively well with measurements, with a MAE of 0.042 (7.9%) and 0.050 (9.4%) for RW and MK datasets, respectively. Both models underestimated DGP, with an MBE of -0.032 and -0.024, respectively. In c+a+ cases, RW model had a MAE of 0.058 (8.70%) and a MBE of -0.049 (-7.30%); MK model had a MAE of 0.064 (9.60%) and MBE of -0.063 (-9.50%). In c+a-cases, RW model had a MAE of 0.032 (7.80%) and MBE of -0.025 (-6.20%); MK model had a MAE of 0.043 (10.6%) and MBE of 0.0059 (1.40%). In c-cases, RW model had a MAE of 0.024 (3.70%) and MBE of 0.015 (2.30%); MK model had a MAE of 0.022 (3.40%) and MBE of -0.011 (-1.70%). DGP error and distribution for each contrast-adaptation condition is shown in Fig. 8 (bottom) and Fig. 9.

When predicting binary glare classification, where $\text{DGP} = 0.38$ is the threshold between no-glare and glare, both analytical models performed relatively well. All high-adaptation condition data points (c+a+ and c-a+) were in the glare category, while low-adaptation condition data points (c+a- and c-a-) were in the glare/no-glare span. The high-adaptation condition had a minimum E_v of 3000 lx and minimum DGP of 0.3361 (Equation (6)). For the high-adaptation condition, both models had a true positive rate and true negative rate of 1.0. For the c+a-condition, the true positive rates were 0.97 and 1.0 for the RW and MK models, respectively; however, RW performed significantly better than MK in the true negative rate: 0.96 and 0.48, respectively. $L_{s,e}$ error for each contrast-adaptation condition is shown in Fig. 8 (top).

Both analytical models showed relative high uncertainty in determining the imperceptible ($\text{DGP} \leq 0.34$), perceptible ($0.34 < \text{DGP} \leq 0.38$), disturbing ($0.38 < \text{DGP} \leq 0.45$), and intolerable ($\text{DGP} > 0.45$) glare categories [21]. The $\text{DGP} \leq 0.45$ range had 143 data points, of which 139 data points were under the c+a-condition, with a MAE of 0.037 (10.2%) and 0.052 (14.3%), and MBE of -0.029 (-7.9%) and 0.026 (7.2%), for the RW and MK models, respectively (Fig. 10, Fig. 11 f, l). Because a MAE of 0.037 and 0.052 is more than half the size of the intervals in the four-point discomfort glare scale, the two models were not sufficient to differentiate between these glare categories.

4. Discussion

Based on the field evaluation with a limited range in AOs and

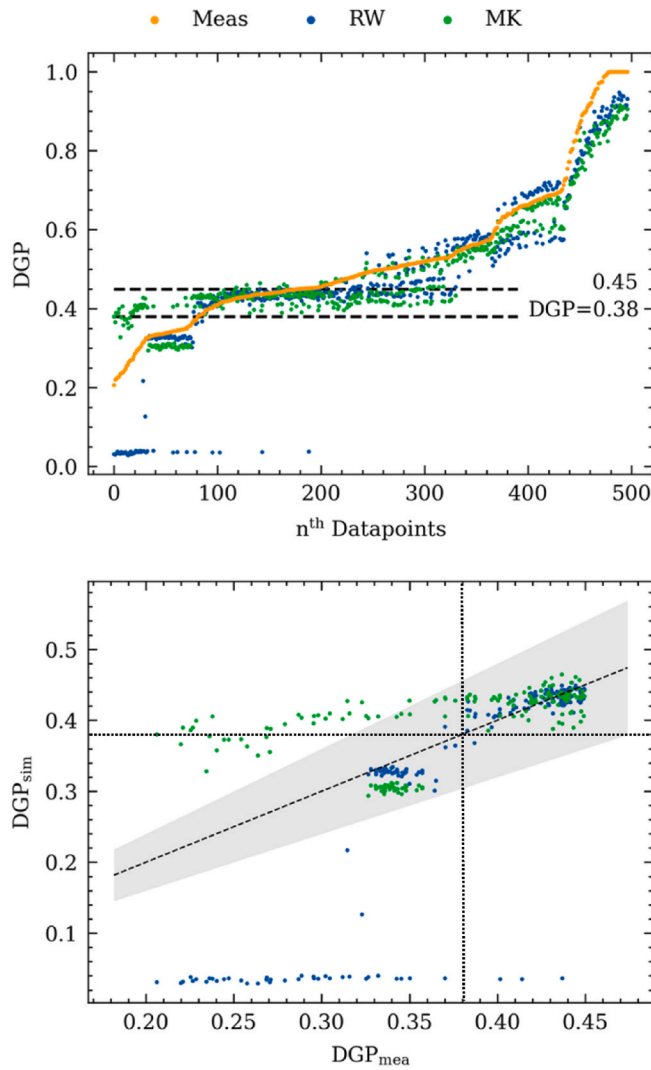


Fig. 10. All measured and simulated RW and MK DGP data points sorted by measured DGP in ascending order along the x-axis (top) with zoom-in at the critical range of $DGP \leq 0.45$ (bottom). The DGP threshold for the binary glare classification was 0.38 and for intolerable glare was 0.45.

comparisons with pgII-derived transmission data (all AOIs), we concluded that for fabrics that created:

c+a+ scenarios

RW performed slightly better than MK in E_v , with a MAE (13.1% vs 14.6%). Both models had an acceptable E_v error (RMSE <32%, MBE <20%) [30,31]. Both models showed similar performance in predicting solar luminance, with a MAE of 18% for both $L_{s,2.5^\circ}$ and $L_{s,5.0^\circ}$. Both models also performed similarly in predicting DGP, with a MAE of 0.058 (8.7%) and 0.064 (9.6%) for RW and MK, respectively. Both models also had a true positive and true negative rate of 1.0. All measured DGP values for c+a+ conditions were greater than 0.4, where errors are of less significance due to high discomfort glare despite high adaptation levels.

c+a-scenarios

RW performed better than MK in E_v with a MAE of 13.7%, as opposed to MK's MAE of 19.2%. E_v errors from both models were still within acceptable range. Both models had a L_s MAE of 35%–40% with RW performing slightly better than MK. RW performed better than MK in predicting DGP with a MAE of 0.032 (7.8%), as opposed to MK's 0.043 (10.6%). RW underestimated DGP with an MBE of -0.025 (-6.20%), whereas MK slightly overestimated DGP with an MBE of 0.0059 (1.40%). RW also performed significantly better than MK in the binary glare classification: true positive rates for both were 100%, but the true negative rate for RW was 96% while MK was 48%. DGP errors under the c+a-condition had more significant implications because this condition covered glare ratings from imperceptible to disturbing.

c-scenarios

Both models performed well in predicting E_v with a similar MAE of 5%. L_s errors were large with a MAE of 139%–236% for $L_{s,2.5^\circ}$, but the errors were likely caused by fabric differences. DGP agreement was similar for the two models with a MAE of 3.5%. Both models had the same true positive and true negative rate of 100%. Because of low contrast conditions, the large L_s error had a relatively smaller implication on predicting visual comfort, whereas E_v played a more significant role (Equation (6)).

Overall, both models could be used to compute E_v and other performance metrics that rely on E_v accuracy more than other factors, such as simplified DGP for low-contrast (c-) conditions. Also, results showed that both models could be used to compute DGP and predict binary glare for the high-adaptation condition (c+a+) because under this condition the occupants are very likely to experience intolerable glare ($DGP > 0.45$) and the true positive rate was 1.0. For the low-adaptation condition, both models were inadequate for category DGP prediction; however, RW was sufficient for the binary glare classification.

4.1. Implication of isotropy

Both MK and RW models were isotropic, i.e., transmittance varied independent of changes in ϕ . For fabrics that exhibited little anisotropic properties, e.g., BL3 (Table 4), an isotropic model could provide sufficient accuracy. However, for fabrics that exhibited pronounced anisotropic properties, such as BD1 shown in Fig. 1, an isotropic model is likely insufficient for all angles of incidence. This was exemplified with sigma metric's poor correlation to MAE in Section 3.1.3 (although RW well outperformed MK) but was difficult to distinguish in field evaluation due to the limited AOI test range.

4.2. Fabric sample differences

The manufacturer provided a large and small sample of each fabric. The large sample was used for the field study and the small sample was used for pgII-derived reference data and as input to the MK and RW analytical models. To assess possible discrepancies between the two samples, both were re-measured using a spectrophotometer with an integrating sphere attachment (PerkinElmer Lambda 950) according to the EN14500 protocol. Even though the two samples were from the same batch in the production line, there were differences in $\tau_{v, n-h}$ and $\tau_{v, n-n}$ between the two samples (Fig. 12). Some fabrics showed little difference between the two samples, while others showed relatively large

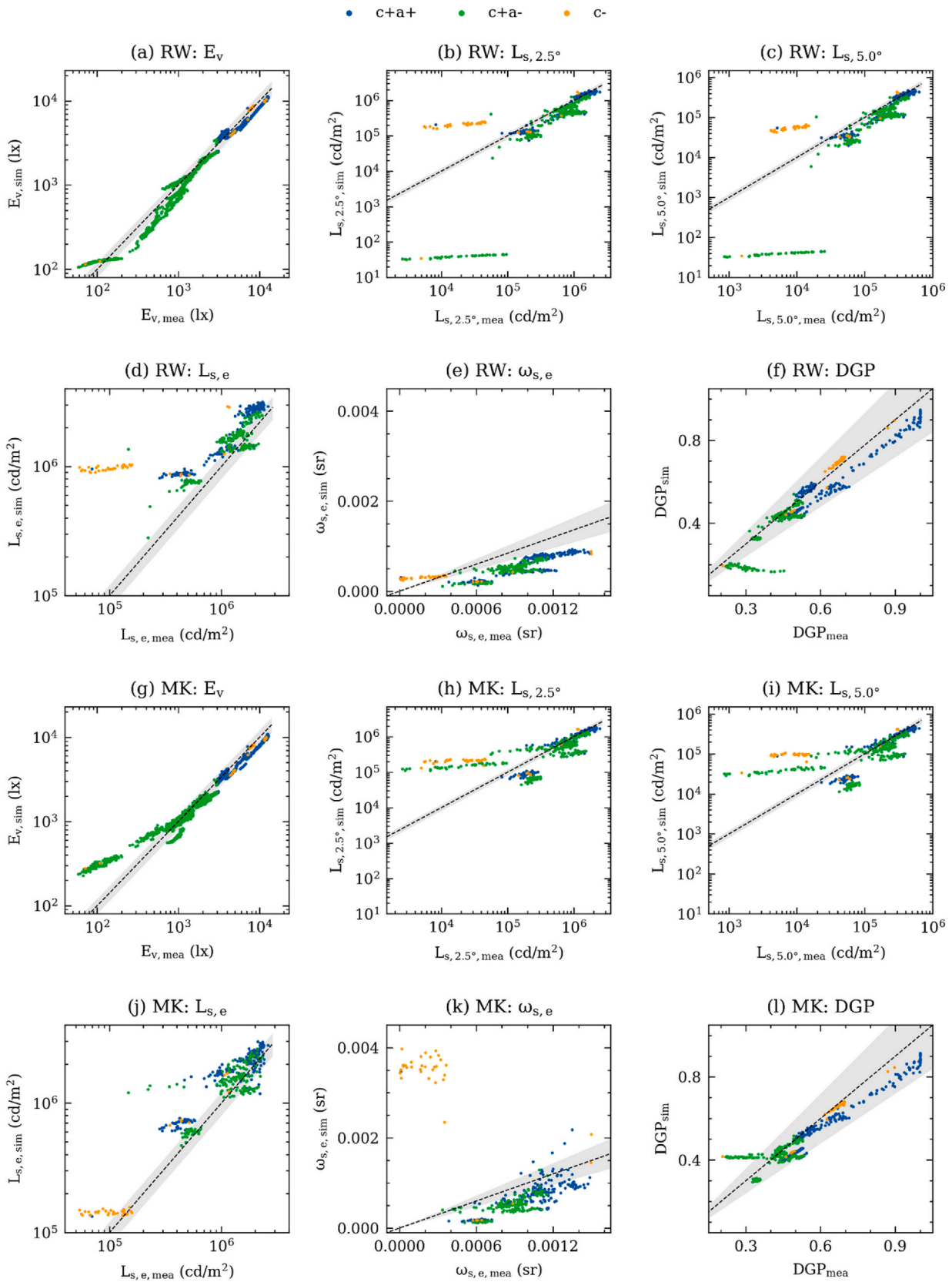


Fig. 11. Overall E_v , solar luminance evaluated at 0.53° and 2.5° apex angles, peak glare source (solar) luminance, solid angle, and DGP agreements between measured (x-axis) and simulated (y-axis) data for the RW (a–f) and MK (g–l) datasets. BD1 was not included in the peak source (solar) luminance and solid angle plots because the solar disk was not in the field of view in the rendered RW model HDR. The shaded area denotes an error range of $\pm 20\%$.

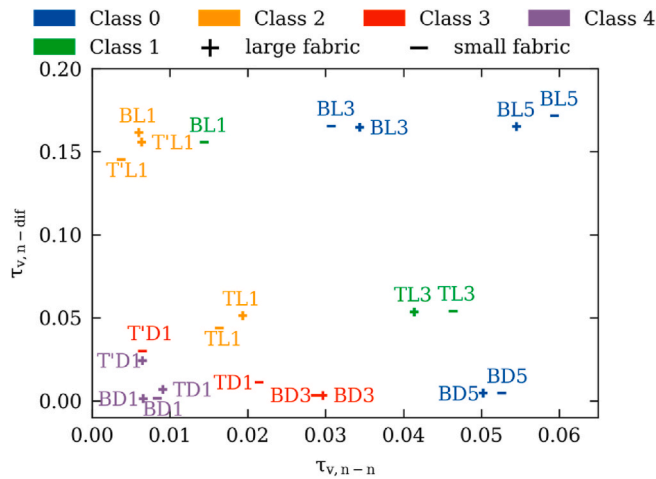


Fig. 12. The eleven fabrics' $\tau_{v, n-n}$ and $\tau_{v, n-dif}$ measured with an integrating sphere instrument. The "+" symbol represents the large fabric sample corresponding field-measured results, while the "-" symbol represents the small fabric sample corresponding to MK and RW simulated results. The colored legend indicates the glare control classification given in Table E.3 of the EN 17037 Standard and Table 7 of EN 14501, where Class 0 has very little effect and Class 4 has a very good effect on control of discomfort glare.

deviations. Some fabrics' large and small samples were in different shading classes (EN17037), e.g., TD1, T'D1 and BL1. For example, the large sample of BL1 had a much smaller $\tau_{v, n-n}$ than the smaller sample. This difference could partially explain why BL1 had no visible through component from the field HDR measurement, whereas the small sample was determined with pgII data to have a specular component, leading to overestimation of L_s shown in Sections 3.2.2 and 3.2.3.

4.3. Cut-off angle determination

The RW model results depended heavily on the maximum directional cut-off angle (χ_{dir}). When compared to pgII-derived values, the RMSE of $\tau_{v, dir-h}(\theta, \varphi)$ using χ_{dir} derived from $\tau_{v, dir-cone(5^\circ)}(\theta, \varphi)$ threshold of 0 and 0.005 were 6.8% and 4.4%, respectively (Fig. 1). The RMSE of $\tau_{v, dir-cone(5^\circ)}(\theta, \varphi)$ simulated with $\tau_{v, dir-cone(5^\circ)}(\theta, \varphi) = 0$ or 0.005 threshold was 79.4% and 18.7%, respectively. $\tau_{v, dir-h}(\theta, \varphi)$ was positively correlated to E_v , while $\tau_{v, dir-cone(5^\circ)}(\theta, \varphi)$ was positively correlated to L_s . Note that despite the lower RMSE, the determination of cut-off angle based on the EN14500-designated 0.005 threshold still resulted in a large underestimation of L_s and DGP for the RW model under the challenging c+a- condition.

4.4. Measurement requirements

While RW performed better than MK, it also required significantly more measurements than MK. As described in EN14500, a fabric's maximum cut-off angle needs to be derived from measurement cut-off angles at multiple ϕ angles, depending on the symmetry properties of the fabric. Determining the cut-off angle for each φ angle requires measuring $\tau_{v, dir-dir}(\theta)$ continuously over θ until the transmission value is smaller than 0.005. A fabric defaults to a 90° cut-off angle if the cut-off angle is not measured. On the other hand, MK only requires a single normal incidence measurement of $\tau_{v, n-h}$, $\tau_{v, n-dif}$, $\rho_{v, f, n-h}$, and $\rho_{v, b, n-h}$. The measurement requirements of the RW model can hinder its adoption for characterizing fabrics at scale.

4.5. Potential improvements

The RW model can be improved by utilizing the cut-off angle data

derived for each requisite φ angle. Instead of using a maximum cut-off angle to derive an isotropic model, the cut-off angle derived at each φ angle can be used to establish an anisotropic model, addressing the issue raised in Section 4.1. The MK model was derived originally for solar and thermal and not for visible and daylight calculation. Re-deriving the model for visible spectra and daylighting calculation, including cut-off angle as a parameter, could also potentially improve its accuracy.

5. Conclusions

Based on the results from this validation study, we concluded that the RW and MK models are sufficient for illuminance-based studies but insufficient for luminance-based studies. BSDF data for about 500 roller shade fabrics of similar weave have been generated using the MK model and are available in the LBNL CGDB library (i.e., entries are certified by AERC 1.0). These entries are sufficient for evaluation of daylight illuminance metrics (E_v , E_h , sDA, ASE). For discomfort glare under high-adaptation and low- or high-contrast (c+a+ and c-a+), as defined by DGP, the RW model was significantly more accurate than the MK model. For discomfort glare under high-contrast and low-adaptation (c+a-), the RW model was again more accurate; it was able to predict binary classification (glare versus no-glare) with a true positive rate of 1.0 and true negative rate of 0.97 whereas the MK model had a true positive rate of 1.0 but only a true negative rate of 0.47. The RW model is sufficient for binary glare classification, while the MK model is not. Both models were insufficient in predicting glare on a four-point scale. The better performance of the RW model could be attributed to the additional χ_{dir} parameter, modeling the fabric cut-off angle. Although RW model required significantly more measurements, it was more accurate than the MK model. Both analytic models were less accurate if the fabric exhibited significant anisotropic behavior. Variations in weave of fabric samples contributed to model error.

CRedit authorship contribution statement

Taoning Wang: Writing – review & editing, Writing – original draft, Methodology, Formal analysis. **Eleanor S. Lee:** Writing – review & editing, Methodology, Formal analysis, Conceptualization. **Gregory J. Ward:** Writing – review & editing, Software. **Tammie Yu:** Writing – review & editing, Visualization, Data curation.

Declaration of competing interest

The authors declare that they have no known competing financial interests or personal relationships that could have appeared to influence the work reported in this paper.

Data availability

Data will be made available on request.

Acknowledgments

This work was supported by the Assistant Secretary for Energy Efficiency and Renewable Energy, Building Technologies Office of the U.S. Department of Energy under Contract No. DE-AC02-05CH11231 and by the California Energy Commission under the Electric Program Investment Charge (EPIC) Program, Solicitation Number: PON-13-301, entitled "Developing A Portfolio of Advanced Efficiency Solutions: Technologies and Approaches for More Affordable and Comfortable Buildings", that was awarded to Lawrence Berkeley National Lab for the work herein.

Appendix

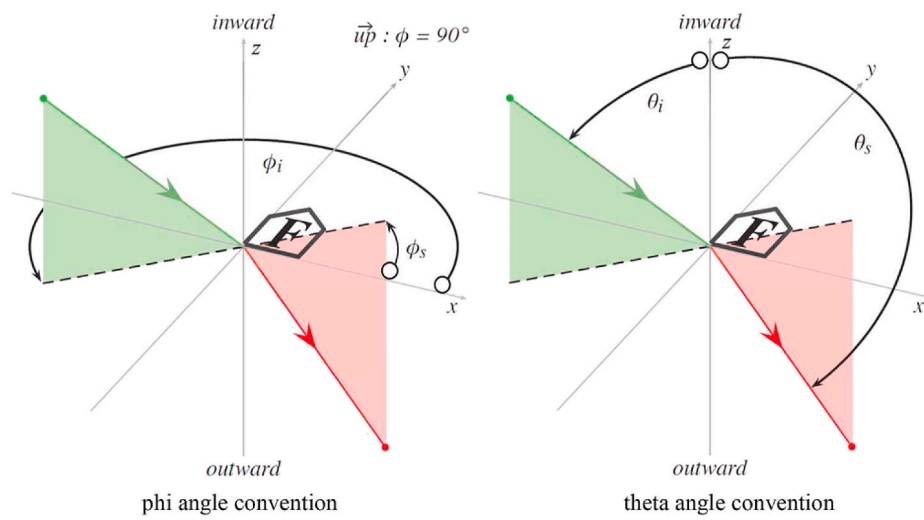


Fig. A.1. Radiance convention for BSDF coordinates: θ , φ , where the “front” (F symbol) of the sample in the x-y plane faces towards the indoors (inward surface normal z-axis); i.e., $\theta_i = 0\text{--}90^\circ$ for incident angles and $\theta_s = 90\text{--}180^\circ$ for outward scattering angles are measured from the inward z-axis; φ_i and φ_s are measured from the x-axis in the x-y plane, where $\varphi = 0^\circ$ points horizontally to the right and $\varphi = 90^\circ$ points upwards when viewing the front of the sample. Source: [HSLU, 24]

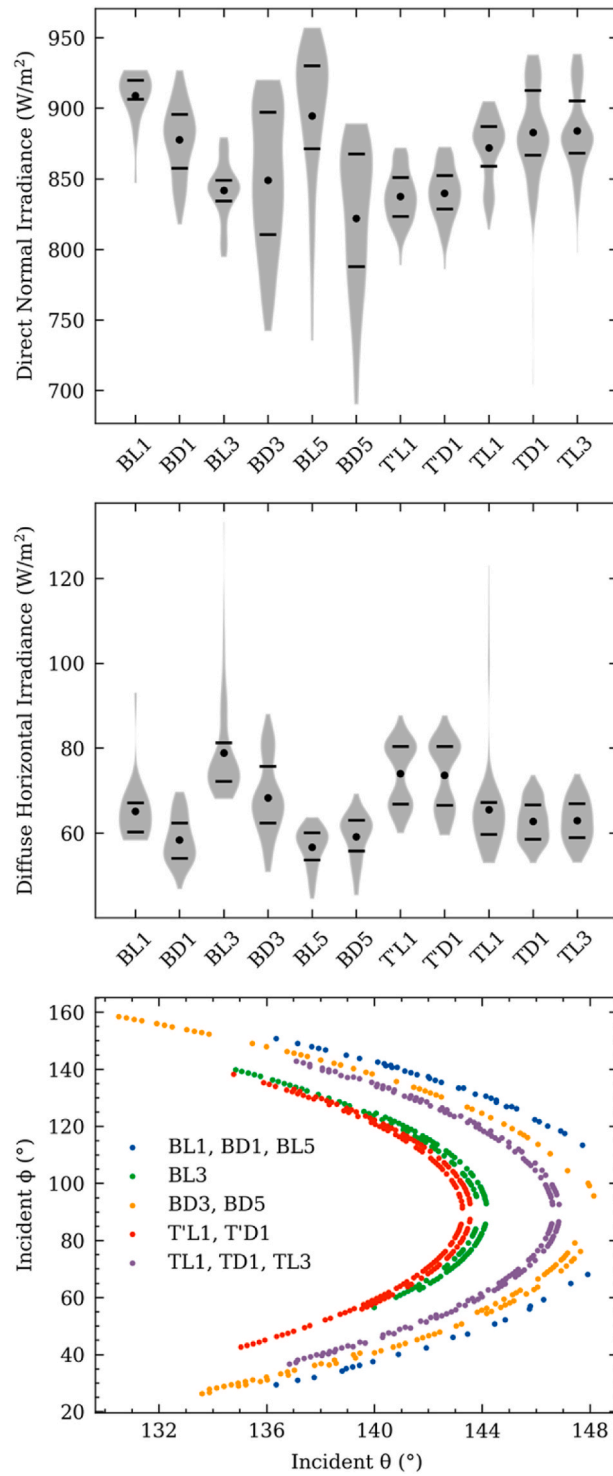


Fig. A.2. The direct normal irradiance (DNI) and diffuse horizontal irradiance (DHI) of all the measured datapoints, which were collected under clear sky conditions. DNI ranged from 690 W/m² to 957 W/m²; DHI ranged from 44 W/m² to 133 W/m². The range of incident $\theta = 130\text{--}150^\circ$ and incident $\phi = 30\text{--}160^\circ$.

Table A.1
E_v (lx) error

	Data count	r ²	RMSE	nRMSE	MAE	nMAE	MBE	nMBE
RW								
All	2066	0.98	681.2	18.2%	468.8	12.5%	-345.5	-9.23%
c+a+	871	0.98	1010.	15.4%	860.6	13.1%	-652.5	-9.92%
c+a-	1111	0.96	205.3	16.8%	167.5	13.7%	-132.5	-10.8%

(continued on next page)

Table A.1 (continued)

	Data count	r^2	RMSE	nRMSE	MAE	nMAE	MBE	nMBE
c-	84	0.93	526.5	6.88%	391.2	5.11%	20.40	0.266%
MK								
All	2066	0.99	837.9	22.4%	548.2	14.6%	-475.1	-12.7%
c+a+	871	0.98	1231.	18.7%	963.6	14.7%	-936.4	-14.2%
c+a-	1111	0.92	295.9	24.2%	235.4	19.2%	-121.5	-9.92%
c-	84	0.93	634.1	8.28%	378.8	4.95%	-367.9	-4.81%

Table A2
 $L_{s,2.5^\circ}$ (cd/m²) error

	Data count	r^2	RMSE	nRMSE	MAE	nMAE	MBE	nMBE
RW								
All	497	0.84	279,085	36.4%	204,857	26.7%	-151,803	-19.8%
c+a+	203	0.87	268,929	25.2%	189,787	17.8%	-136,843	-12.8%
c+a-	256	0.79	295,362	47.3%	219,289	35.1%	-210,036	-33.6%
c-	38	0.84	211,243	181.1%	188,139	161.1%	160,593	137.1%
MK								
All	497	0.80	293,369	38.2%	217,522	28.3%	-126,682	-16.5%
c+a+	203	0.87	268,098	25.1%	183,328	17.2%	-131,521	-12.3%
c+a-	256	0.61	322,243	51.6%	248,981	39.9%	-166,280	-26.6%
c-	38	0.88	205,214	176.1%	188,258	161.1%	165,938	142.1%

Table A3
 $L_{s,5.0^\circ}$ (cd/m²) error:

	Data count	r^2	RMSE	nRMSE	MAE	nMAE	MBE	nMBE
RW								
All	497	0.85	7,3692	37.1%	55,104	27.7%	-43,490	-21.9%
c+a+	203	0.87	71,465	25.8%	51,483	18.6%	-41,417	-15.0%
c+a-	256	0.80	78,127	48.4%	59,280	36.7%	-57,288	-35.5%
c-	38	0.84	51,194	154.1%	46,320	139.1%	38,391	115.1%
MK								
All	497	0.78	78,484	39.5%	59,703	30.1%	-33,382	-16.8%
c+a+	203	0.87	70,559	25.5%	49,371	17.9%	-38,064	-13.8%
c+a-	256	0.61	83,688	51.8%	65,104	40.3%	-45,307	-28.1%
c-	38	0.74	82,368	247.1%	78,517	236.1%	71,970	216.1%

Table A4
 $L_{s,e}$ (cd/m²) error:

	Data count	r^2	RMSE	nRMSE	MAE	nMAE	MBE	nMBE
RW								
All	457	0.78	559,088	45.4%	480,690	39.0%	434,493	35.3%
c+a+	203	0.88	646,073	45.1%	593,738	41.5%	567,167	39.6%
c+a-	217	0.73	361,784	29.8%	311,441	25.6%	239,007	19.7%
c-	37	0.64	896,119	407.1%	853,080	387.1%	853,080	387.1%
MK								
All	457	0.73	442,942	36.0%	357,739	29.1%	251,937	20.5%
c+a+	203	0.74	489,669	34.2%	430,505	30.1%	329,140	23.0%
c+a-	217	0.49	428,854	35.3%	333,865	27.5%	206,173	17.0%
c-	37	0.95	170,687	77.4%	98,527.0	44.7%	96,760.1	43.9%

Table A5

 $\omega_{s,e}$ (sr) error:

	Data count	r^2	RMSE	nRMSE	MAE	nMAE	MBE	nMBE
RW								
All	457	0.67	0.000410	47.5%	0.000390	45.2%	-0.000370	-42.9%
c+a+	203	0.79	0.000440	43.9%	0.000420	41.9%	-0.000420	-41.9%
c+a-	217	0.69	0.000400	48.5%	0.000390	47.2%	-0.000390	-47.2%
c-	37	0.61	0.000260	82.4%	0.000200	63.4%	0.000014	4.44%
MK								
All	457	0.11	0.000960	111.%	0.000560	64.9%	-0.000080	-9.27%
c+a+	203	0.32	0.000450	44.8%	0.000360	35.9%	-0.000290	-28.9%
c+a-	217	0.44	0.000380	46.0%	0.000360	43.6%	-0.000350	-42.4%
c-	37	0.43	0.003100	983.%	0.002800	888.%	0.002700	856.%

Table A6

DGP error:

	Data count	r^2	RMSE	nRMSE	MAE	nMAE	MBE	nMBE
RW								
All	497	0.93	0.059	11.1%	0.042	7.88%	-0.032	-6.01%
c+a+	203	0.95	0.067	10.0%	0.058	8.70%	-0.049	-7.35%
c+a-	256	0.74	0.056	13.7%	0.032	7.83%	-0.025	-6.11%
c-	38	0.97	0.026	4.01%	0.024	3.70%	0.015	2.31%
MK								
All	497	0.91	0.067	12.6%	0.050	9.39%	-0.024	-4.51%
c+a+	203	0.96	0.076	11.4%	0.064	9.59%	-0.063	-9.44%
c+a-	256	0.29	0.063	15.4%	0.043	10.5%	0.0059	1.44%
c-	38	0.88	0.041	6.32%	0.022	3.39%	-0.011	-1.69%

References

- [1] U.S. DoE, Buildings energy data book, *Energy Effic. Renew. Energy* (2011).
- [2] J. Wienold, J. Christoffersen, Evaluation methods and development of a new glare prediction model for daylight environments with the use of CCD cameras, *Energy Build.* 38 (7) (2006) 743–757, <https://doi.org/10.1016/j.enbuild.2006.03.017>.
- [3] G.J. Ward, T. Wang, D. Geisler-Moroder, E.S. Lee, L.O. Grobe, J. Wienold, J. C. Jonsson, Modeling specular transmission of complex fenestration systems with data-driven BSDFs, *Build. Environ.* 196 (2021), 107774, <https://doi.org/10.1016/j.buildenv.2021.107774>.
- [4] S. Wasilewski, L.O. Grobe, J. Wienold, M. Andersen, Efficient simulation for visual comfort evaluations, *Energy Build.* 267 (2022), 112141, <https://doi.org/10.1016/j.enbuild.2022.112141>.
- [5] G.J. Ward, B. Bueno, D. Geisler-Moroder, L.O. Grobe, J.C. Jonsson, E.S. Lee, H. R. Wilson, Daylight simulation workflows incorporating measured bidirectional scattering distribution functions, *Energy Build.* 259 (2022), 111890, <https://doi.org/10.1016/j.enbuild.2022.111890>.
- [6] T. Wang, E.S. Lee, G.J. Ward, T. Yu, Field validation of data-driven BSDF and peak extraction models for light-scattering fabric shades, *Energy Build.* 262 (2022), 112002, <https://doi.org/10.1016/j.enbuild.2022.112002>.
- [7] D. Geisler-Moroder, P. Apian-Bennewitz, J. de Boer, B. Deroisy, Y. Fang, Y. Wu, Analysis and Evaluation of BSDF Characterization of Daylighting Systems. T61. C. 2.2–A Technical Report of Subtask C, IEA SHC Task 61/EBC Annex 77, 2021.
- [8] E.S. Lee, D. Geisler-Moroder, G. Ward, Modeling the direct sun component in buildings using matrix algebraic approaches: methods and validation, *Sol. Energy* 160 (2018) 380–395, <https://doi.org/10.1016/j.solener.2017.12.029>.
- [9] P. Apian-Bennewitz, J. Von Der Hardt, Enhancing and calibrating a goniophotometer, *Sol. Energy Mater. Sol. Cell.* 54 (1–4) (1998) 309–322, [https://doi.org/10.1016/S0927-0248\(98\)00082-8](https://doi.org/10.1016/S0927-0248(98)00082-8).
- [10] L.O. Grobe, S. Wittkopf, P. Apian-Bennewitz, J.C. Jonsson, M. Rubin, Experimental validation of bidirectional reflection and transmission distribution measurements of specular and scattering materials, in: *Photonics for Solar Energy Systems III*, vol. 7725, SPIE, 2010, May, pp. 256–274, <https://doi.org/10.1117/12.854011>.
- [11] P. Apian-Bennewitz, Design and construction of a device for measuring light-scattering on anisotropic materials, *arXiv* (2021), <https://doi.org/10.48550/arXiv.2105.15112> preprint arXiv:2105.15112.
- [12] I. Konstantzos, Y.C. Chan, J.C. Seibold, A. Tzempelikos, R.W. Proctor, J. B. Protzman, View clarity index: a new metric to evaluate clarity of view through window shades, *Build. Environ.* 90 (2015) 206–214, <https://doi.org/10.1016/j.buildenv.2015.04.005>.
- [13] G. Flamant, W. Bustamante, A. Tzempelikos, S. Vera, Evaluation of view clarity through solar shading fabrics, *Build. Environ.* 212 (2022), 108750, <https://doi.org/10.1016/j.buildenv.2021.108750>.
- [14] W.H. Ko, S. Schiavon, S. Altomonte, M. Andersen, A. Batool, W. Browning, J. Wienold, Window view quality: why it matters and what we should Do, *Leukos* 18 (3) (2022) 259–267, <https://doi.org/10.1080/15502724.2022.2055428>.
- [15] E.S. Lee, B.S. Matusiak, D. Geisler-Moroder, S.E. Selkowitz, L. Heschong, Advocating for view and daylight in buildings: next steps, *Energy Build.* 265 (2022), 112079, <https://doi.org/10.1016/j.enbuild.2022.112079>.
- [16] Attachments Energy Rating Council, AERC 1.1, procedures for determining the optical and thermal properties of window attachment materials. <https://aercenergyrating.org/wp-content/uploads/2023/02/AERC-1.1-Revision-5.pdf>, 2018. (Accessed 1 March 2023).
- [17] A. Tzempelikos, Y.C. Chan, Estimating detailed optical properties of window shades from basic available data and modeling implications on daylighting and visual comfort, *Energy Build.* 126 (2016) 396–407, <https://doi.org/10.1016/j.enbuild.2016.05.038>.
- [18] Y.-C. Chan, A. Tzempelikos, I. Konstantzos, A systematic method for selecting shading properties for glare protection, *Energy Build.* 92 (2015) 81–94, <https://doi.org/10.1016/j.enbuild.2015.01.057>.
- [19] J. Jonsson, E.S. Lee, M.D. Rubin, Light-scattering properties of a woven shade-screen material used for daylighting and solar heat-gain control, in: *Proceedings of SPIE Conference, Reflection, Scattering, and Diffraction from Surfaces*, August, 2008, 70650R, <https://doi.org/10.1117/12.795575>.
- [20] J. Wienold, T.E. Kuhn, J. Christoffersen, M. Andersen, *Annual Glare Evaluation for Fabrics PLEA 2017*, 2017. Edinburgh, July 3–5, 2017.
- [21] J. Wienold, T. Iwata, M. Sarey Khanie, E. Erell, E. Kaftan, R.G. Rodriguez, M. Andersen, Cross-validation and robustness of daylight glare metrics, *Light. Res. Technol.* 51 (7) (2019) 983–1013, <https://doi.org/10.1177/14771535198260>.
- [22] S. Jain, C. Karmann, J. Wienold, Behind electrochromic glazing: assessing user's perception of glare from the sun in a controlled environment, *Energy Build.* 256 (2022), 111738, <https://doi.org/10.1016/j.enbuild.2021.111738>.
- [23] A. Roos, P. Polato, P.A. Van Nijntenn, M.G. Hutchins, F. Olive, C. Anderson, Angular-dependent optical properties of low-e and solar control windows: simulations versus measurements, *Sol. Energy* 69 (2001) 15–26, [https://doi.org/10.1016/S0038-092X\(01\)00019-6](https://doi.org/10.1016/S0038-092X(01)00019-6).
- [24] N.A. Kotey, *Measurements and Models Related to Solar Optics in Windows with Shading Devices*, PhD thesis, University Waterloo, 2009.
- [25] G. Ward, A practical framework for sharing and rendering real-world bidirectional scattering distribution functions. <https://doi.org/10.2172/1172245>, 2012.
- [26] D. Geisler-Moroder, G.J. Ward, T. Wang, E.S. Lee, Peak extraction in daylight simulations using BSDF data, in: *Proceedings of Building Simulation, 2021*, pp. 1–3, <https://doi.org/10.26868/25222708.2021.30374>.
- [27] R. Perez, R. Seals, J. Michalsky, All-weather model for sky luminance distribution—preliminary configuration and validation, *Sol. Energy* 50 (3) (1993) 235–245, [https://doi.org/10.1016/0038-092X\(93\)90017-1](https://doi.org/10.1016/0038-092X(93)90017-1).

- [28] J. Wienold, M. Andersen, Evalglare 2.0—new features, faster and more robust HDR-image evaluation, in: *In the 15th International Radiance Workshop, 2016 (Padova, Italy)*.
- [29] G. Quek, J. Wienold, M.S. Khanie, E. Ereil, E. Kaftan, A. Tzempelikos, M. Andersen, Comparing performance of discomfort glare metrics in high and low adaptation levels, *Build. Environ.* 206 (2021), 108335, <https://doi.org/10.1016/j.buildenv.2021.108335>.
- [30] C. Reinhart, P.F. Breton, Experimental validation of Autodesk® 3ds Max® design 2009 and DAYSIM 3.0, *Leukos* 6 (1) (2009) 7–35.
- [31] N.L. Jones, C.F. Reinhart, Experimental validation of ray tracing as a means of image-based visual discomfort prediction, *Build. Environ.* 113 (2017) 131–150, <https://doi.org/10.1016/j.buildenv.2016.08.023>.